RSC Advances

PAPER

View Article Online
View Journal | View Issue

Cite this: *RSC Adv.*, 2023, **13**, 15437

Insight into the structural, optoelectronic, and thermoelectric properties of Fe_2HfSi Heusler by DFT investigation

Abida Azam,[a] Ramesh Sharma, *[b] Debidatta Behera,[c] Hafiz Hamid Raza,[a] H. Saad Ali,[a] Shaimaa A. M. Abdelmohsen,[d] Ashraf M. M. Abdelbacki[e] and Sanat Kumar Mukherjee[c]

At high pressure, the pressure dependencies of the structural, electronic, optical, and thermoelectric properties of Fe_2HfSi Heusler were calculated using the FP-LAPW method within the framework of the density functional theory. The calculations were carried out using the modified Becke–Johnson (mBJ) scheme. Our calculations showed that the Born mechanical stability criteria confirmed the mechanical stability in the cubic phase. Further, through Poisson and Pugh's ratios critical limits, the findings of the ductile strength were computed. At a pressure of 0 GPa, the indirect nature of the material may be deduced from the electronic band structures of Fe_2HfSi as well as the estimations for its density of states. Under pressure, the real and imaginary dielectric function responses, optical conductivity, absorption coefficient, energy loss function, refractive index, reflectivity, and extinction coefficient were computed in the 0–12 eV range. Using semi-classical Boltzmann theory, a thermal response is also studied. As the pressure rises, the Seebeck coefficient decreases, while the electrical conductivity rises. The figure of merit (*ZT*) and Seebeck coefficients were determined at temperatures of 300 K, 600 K, 900 K, and 1200 K in order to better understand the thermoelectric properties of a material at these different temperatures. Despite the fact that the ideal Seebeck coefficient for Fe_2HfSi was discovered at 300 K and was determined to be superior to that reported previously. Materials with a thermoelectric reaction has been shown to be suitable for reusing waste heat in systems. As a result, Fe_2HfSi functional material may aid in the development of new energy harvesting and optoelectronic technologies.

Received 17th January 2023
Accepted 8th March 2023

DOI: 10.1039/d3ra00362k

rsc.li/rsc-advances

1. Introduction

The serious threat to our society is day-by-day increasing due to the increased demand for energy caused by the deterioration of fossil fuels in addition to hazardous elements increasing in the environment leading to global warming. It turns the world's interest in renewable sources of energy. The direct conversion between thermal and electrical energies known to be thermoelectricity is a very promising way for renewable energy generation through which the wasted heat of the system can be beneficial to meet needs.[1,2] The efficiency of thermoelectric (TE) materials can be described by their known parameter figure of merit (*ZT*), which can be defined with the expression $ZT = (S^2\sigma T)/(\kappa_e + \kappa_l)$, where S is the thermos-power (Seebeck coefficient), σ is electrical conductivity, T is absolute temperature, and κ_e and κ_l are the electronic and lattice contributions, respectively, to the thermal conductivity. More than fifty years ago with the discovery of Bi_2Te_3-based alloys heaving $ZT \sim 1$,[3] though $ZT > 3$ for TE devices in comparison to becoming more efficient than other energy conservation resources, still a challenge to achieve high *ZT*. Among the various TE materials, chalcogenides,[4,5] skutterudites,[6,7] and half-Heusler alloys,[8–14] have also emerged as appropriate nominees in the stream. Owing to features, such as phase transitions, strong spin polarization, and half-metallicity for device application TEs and spintronics, Heusler alloys have been the centre of interest in the scientific community.[15–17] Iron-based Heusler alloys have been enormously explored and reported. They have a wide range of electronic structures, from metallic to semiconducting. Experimentally, half-metallic Fe_2YSi (Y = Co, Ni, Mn, Cr, and Fe) compounds were produced.[18] Other research groups examined iron-based half-metallic compounds that were in great demand for TE device production, such as Fe_2YZ (Z = Y = Zr, Ta, Hf, V, Ti, and Nb, and Sn, Ge, Si, Al, Ga, and In), and a recent study revealed

[a]*Centre for Advanced Studies in Physics, GC University, Lahore-54000, Pakistan*
[b]*Dept. of Applied Science, Feroze Gandhi Institute of Engineering and Technology, Raebareli-229001, Uttarpradesh, India. E-mail: sharmadft@gmail.com*
[c]*Dept. of Physics, Birla Institute of Technology, Mesra Ranchi, Jharkhand, India*
[d]*Department of Physics, College of Science, Princess Nourah Bint Abdulrahman University, P.O. Box 84428, Riyadh 11671, Saudi Arabia*
[e]*Plant Pathology Department, Faculty of Agriculture, Cairo University, Cairo 12613, Egypt*

a high-power factor at room temperature (RT).[19,20] The TE response of the Fe_2Val material and full Heusler Fe_2ZrSi at 700 K up to 40 GPa have been testified under pressure by S. Masuda *et al.* and Sofi *et al.*, respectively.[21,22] Following this, we investigate the influence of pressure on the TE analysis of L21-type Heusler alloys, which would allow us to gain a better understanding of the numerous factors contributing to the alloy's improved TE response. To the best of our knowledge comprehensive study to calculate structural, electronic, elastic, optical, and transport properties under high pressure of Fe_2HfSi was performed for the first time to reveal the characteristics of the studied half Heusler alloy. This study is divided into sections, Section 1 consists of structural details, Section 2 involves theoretical calculations lastly Section 3 describes the results and detailed discussions along with the summary.

2. Computational approach

First-principles calculations by the Full Potential Linearized Augmented Plane Wave (FP-LAPW) method embedded in the WIEN2k code were used to explore the current study on half Heusler alloy.[23] The electronic configuration of the constituent atoms is as follows: Fe = [Ar] $3d^6$ $4s^2$, Hf = Hf: [Xe] $4f^{14}$ $5d^2$ $6s^2$, Si = [Ne] $3s^2$ $3p^2$. Prior to exploring the findings of experimental results for the materials, the DFT was proven as a key tool for defining the various attributes. The FP-LAPW approach, as implemented in the WEIN2k code, was used to complete the task. By treating the onsite strong correlation of the 3d electrons, we applied the Perdew–Burke–Ernzerhof scheme of the generalised gradient approximation (PBE-GGA) for the exchange-correlation functional.[24] However, the modified Becke–Johnson (mBJ) approach may be used to predict the nature of the band structure at optimized lattice constants.[25] At diverse pressures of 0 GPa, 15 GPa, and 30 GPa the different physical properties were computed. Energy and charge convergence were achieved at 0.0001 Ry and 0.0001*e* respectively, whereas, the plane wave number was obtained as $K_{MAX} = 7.0/R_{MT,}$ and a 5000 *k*-point-mesh was employed. The thermoelectric properties were calculated using the Boltzmann transport theory,[26] with the relaxation time constant for charge carriers approximation. To comprehend the convergence criterion, a compact mesh of 46 × 46 × 46 *k*-points was used.

3. Results and discussion

3.1. Structural properties

Structural characteristics of the studied half Heusler compounds were exposed within pressure dependencies. Fe_2-HfSi structure crystallizes (prototype Cu_2MnAl) in the $Fm\bar{3}m$ space group with Y atom (Hf) occupying 4b (0, 0, 0), Z atom (Si) sit 4a (1/2, 1/2, 1/2) and the 8c (1/4, 1/4, 1/4) position was occupied by the Fe atoms. The optimal crystal structure and total energy as a volume-dependent function were predicted using the Murnaghan equation[27] of state and shown in Fig. 1 is given as.

$$E(V) = E_o + \frac{9V_oB_o}{16}\left\{\left[\left(\frac{V_o}{V}\right)^{\frac{2}{3}} - 1\right]^3 B'_o + \left[\left(\frac{V_o}{V}\right)^{\frac{2}{3}} - 1\right]^2 - 1\left[6 - 4\left(\frac{V_o}{V}\right)^{\frac{2}{3}}\right]\right\} \quad (1)$$

where B, B'_o, and V are the bulk modulus, pressure derivative of the bulk modulus, and volume, respectively. The minimum energy at the optimized volume is found in the ferromagnetic (FM) phase at pressure 0 GPa with a lattice parameter of 5.920 Å and agrees with experimentally/theoretically reported values of 5.884 Å and 5.930 Å at room temperature from the family of these compounds.[22,28,29] The estimated parameters of the examined Heusler compound lattice constant, its pressure derivative, unit cell volume, bulk modulus, minimum ground-state energy, and cohesive energy are presented in Table 1. The comparison[30] shows that the lattice constant increases in Fe_2YSi as the atomic number at Y place changes, a lesser B value anticipates that the studied compound is much easier to press as Fe_2ZrSi.

3.2. Mechanical stability and thermodynamic behavior

The effect of pressure on the mechanical properties of the studied compound was computed employing the IR-elast method[31] implemented in WIEN2k software. In order to de describe the mechanical properties of cubic structured Fe_2HfSi three elastic constants C_{11}, $C_{12,}$ and C_{44} were determined.[31] They were found to satisfy the essential Born mechanical stability criteria expressed as C_{11}–$C_{12} > 0$, $C_{11} < 2C_{12} > 0$, $C_{44} > 0$ and $C_{12} < B < C_{11}$ suggesting mechanical stability. The various elastic constants at different external pressure are represented in Table 2. The elastic constants are observed to increase with pressure. The elastic constants bulk modulus (B), Young modulus (E), and shear modulus (G) were observed to increase with applied pressure, which is associated with the reorientation of the electronic states. Other elastic properties such as Cauchy pressure (C_{11}–C_{12}), Poisson's ratio (y), and Pough's index of ductility (B/G) are computed to estimate the brittle and ductile nature, as shown in Table 2. The Cauchy pressure is noticed to be positive revealing the investigated compound is ductile in nature. Bulk modulus (B) is computed as $B = (C_{11} + 2C_{12})/3$ and is, therefore, a linear combination of C_{12} and C_{11}. The B for the compound under investigation was determined and is given in Table 2. The strong consistency between the bulk moduli of Murnaghan's state equation (Table 1) and the bulk moduli of the elastic constant calculation is an indication of the correctness of the evaluated Fe_2HfSi elastic constants. Moreover, Poisson's ratio (σ) has a critical 0.26. For the ductile nature, its value is more than 0.26 otherwise brittle. For all the applied pressures, it was observed to be brittle in nature, as evidenced by the data in Table 2. The anisotropic factor A is another key parameter that gives information regarding the nature of micro-cracks. The magnitude equal to 1 suggests isotropic nature whereas any deviation from this value suggests anisotropic nature. As

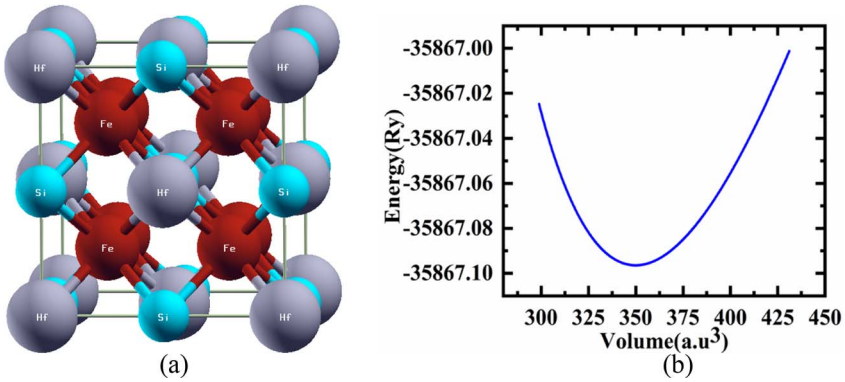

Fig. 1 (a) Crystal structure (b) total energy *versus* volume for Fe_2HfSi.

noticed in Table 2, at all the investigated pressure the compound is anisotropic in nature. The thermodynamic properties of the compounds were calculated by Debye temperature (θ_D) from elastic constants as expressed by relationship.

$$\theta_D = \frac{h}{K_B}\left[\frac{3n}{4\pi}\left(\frac{N_A\rho}{M}\right)\right]^{-1/3} V_m \quad (2)$$

where k is Boltzmann's constant, h Plank's constant, N_A is Avogadro's number, ρ is the density of the material, M is the molecular weight, and n is the number of atoms in a single cell. The estimated Debye temperature is given in Table 2. The mean sound speed of the investigated compound was computed using:

$$V_m = \left[\frac{1}{3}\left(\frac{2}{\vartheta_t{}^3} + \frac{1}{\vartheta_t{}^3}\right)\right]^{-(1/3)} \quad (3)$$

where the longitudinal and transverse components of sound velocity are ϑ_l and ϑ_t, and were calculated using shear modulus and bulk modulus, respectively as:[32]

$$\vartheta_t = \sqrt{\frac{G}{\rho}}\vartheta_l = \sqrt{\frac{3B+4G}{3\rho}} \quad (4)$$

Table 2 provides the computed values of ϑ_t, ϑ_l, V_m, θ_D, and T_m

3.3. Electronic properties

This part of the exploration constitutes the electronic behavior within the material around the Fermi energy (E_F) level. These electronic details are depicted in the electronic band structure and density of electronic states as shown in Fig. 2 and 3, respectively under the chosen pressure range 0–30 GPa. A definite gap between the conduction and valence band is observed that categorized Fe_2ZrSi as semiconducting material. The bands are plotted in the first Brillouin zone (BZ) with a blue dotted line on the energy axis in Fig. 2 showing the E_F while W–L–Γ X–W–K are the high symmetry points in the first BZ.

The conduction band's bottom and the valence band's top do not meet at the same symmetry point, as such is indirect in nature with a small shift in band gap around E_F as pressure increases from 0 GPa to 30 GPa. This variation is exposed in Fig. 3 and also in Fig. 4. That means as pressure increases, the material tends towards more stability. As a result, pressure-induced expansion of the semiconductor heaving indirect bandgap is rather slight. The gap value rises with the addition of mBJ up to 0.6 eV in Fe_2HfSi at $P = 0$ GPa disclosing an increase of more than 33%, as depicted in Table 3.

To explore more about electronic characteristics, the densities of states (DOS) are depicted relative to E_F in Fig. 4, displaying the total and partial densities of state (PDOS) over the specified range of pressure in gigapascal units. The black line indicates the overall contribution of the compound with constituent atoms Fe-3d, Hf-5d, and Si-3p at zero, fifteen, and thirty gigapascals orderly. The s-orbital of Si slightly contributes to electronic investigations of Fe_2HfSi as compared to the other atoms, while the stronger contribution comes from the Fe d-orbital, Hf d-orbital whereas for the Si it is p-orbital. When the pressure is increased, there is very little discernible shift in the profile of the DOS. Moreover, there is a significant disparity in the locations of the peaks. Fe_2HfSi exhibits equal contributions of Fe-3d, Hf-5d, and orbital 3p of the Si at 0–5 eV. Fe-3d is the main contributor to the unoccupied states. For Fe_2HfSi, the DOS matches well with the experimental results reported in literature.[33]

Table 1 The optimized structural parameters for Fe_2HfSi in the FM phase

Compound	a (Å)	V (a.u)^3	B (GPa)	B'_o (GPa)	E_o (Ry)	$E_{cohesive}$
Fe_2HfSi	5.92	350.0209	213.5035	4.1774	−35867.096	
Ref.	6.05 (ref. 28)					
Ref.	5.86 (ref. 27)		353.96 (ref. 22)			

Table 2 Values of elastic constants (C_{ij}), bulk modulus (B), shear modulus (G), Young's modulus (Y), Poisson's ratio (σ), Pugh ratio, Frantsevich ratio, shear anisotropy factor (A) Cauchy pressure C^P, sound velocities (m s^{-1}), Debye temperature θ_D (K) of Fe_2HfSi

Material property	0 GPa	15 GPa	30 GPa
C_{11} (GPa)	383.15	500.74	595.68
C_{12} (GPa)	116.89	155.96	192.17
C_{44} (GPa)	133.93	184.91	223.71
Bulk modulus, B (GPa)	205.65	270.88	326.67
Shear modulus, G (GPa)	133.61	179.79	214.65
Young modulus, Y (GPa)	329.486	441.67	528.81
Poisson ratio, σ (GPa)	0.232	0.228	0.230
Pugh ratio, B/G (GPa)	1.53	1.506	1.521
Frantsevich ratio, G/B (GPa)	0.649	0.663	0.657
Shear anisotropy factor, A (GPa)	1.006	1.150	1.108
Cauchy pressure C^P (GPa)	−17.04	−28.95	−31.54
Transverse sound velocity (m s^{-1})	3617.11	4066.55	4334.17
Longitudinal sound velocity (m s^{-1})	6130.4	6853.02	7323.61
Average sound velocity (m s^{-1})	4007.8	4503.38	4800.95
Temperature θ_D (K)	508.27	583.176	632.10
Melting temperature T_m (K)	2817.47 ± 300 K	3512.39	4073.48

3.4. Optical properties

Materials with suitable optical features play a key role in opto-electronic applications. As optical properties are demonstrated under pressure ranges 0–30 GPa of Fe_2HfSi in cubic phase in this work and plotted in the energy range up to 12 eV. The complex dielectric function $\varepsilon(\omega) = \varepsilon_1(\omega) + i\varepsilon_2(\omega)$[34] with real $\varepsilon_1(\omega)$ and imaginary part $\varepsilon_2(\omega)$ characterizes the linear response of studied material towards incoming electromagnetic radiations, as shown in Fig. 4.

The $\varepsilon_1(\omega)$ component indicates the extent to which a material may be polarised.[35] The static dielectric constant was found to be dependent upon the bandgap (E_g) of the material. While with the pressure climbing from 15 to 30 GPa, the static dielectric function declines, as the actual dielectric function falls and approaches zero at 4.8–5.0 eV. If more energy increases, the dielectric function becomes negative, which made this material might be as that of meta-material as shown in Fig. 4(a).[35,36] By increasing the pressure to 30 GPa, a little movement towards higher energy areas was observed in this graph.

The imaginary part $\varepsilon_2(\omega)$ contributes significantly to defining more about the optical illustration for any material. Greater values correspond to the higher absorption of explored medium. This proposes a deep effect on absorption. Fig. 4(b) depicts the relationship between the imaginary component of the dielectric function and energy, showing how the material's absorption zone thickens as pressure increases. To put it simply, the absorption peaks at 0 GPa and dips at 30 GPa due to indirect bandgap transitions at high symmetry sites between the valence band maximum and conduction band minimum. There also exist some peaks because of the inter-band transitions. To figure out the surface behaviour, the ratio of the incident power to the reflected power is used to figure out reflectivity. The dielectric pattern nearly follows as reported previously.[37] The refractive index and extinction coefficient *versus* energy spectrum are presented in Fig. 4(c) and (d). The static index n (0) values of 4.89, 4.81, and 4.77 may be observed in the figure for cubic Fe_2HfSi at 0, 15, and 30 GPa pressure, respectively. As the pressure rises over 0–30 GPa, the refractive

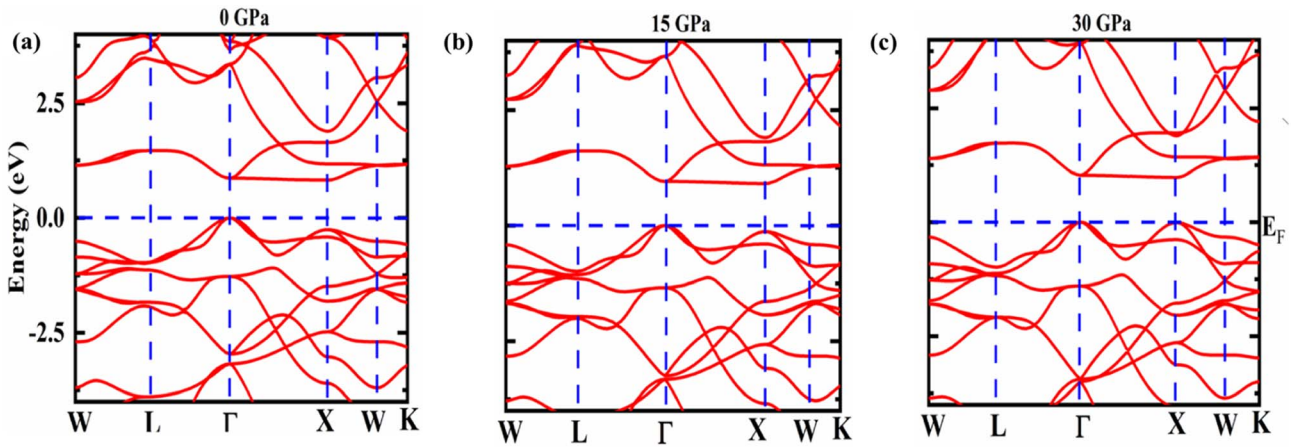

Fig. 2 Band structure of Fe_2HfSi (a) at 0 GPa; (b) at 15 GPa (c) at 30 GPa.

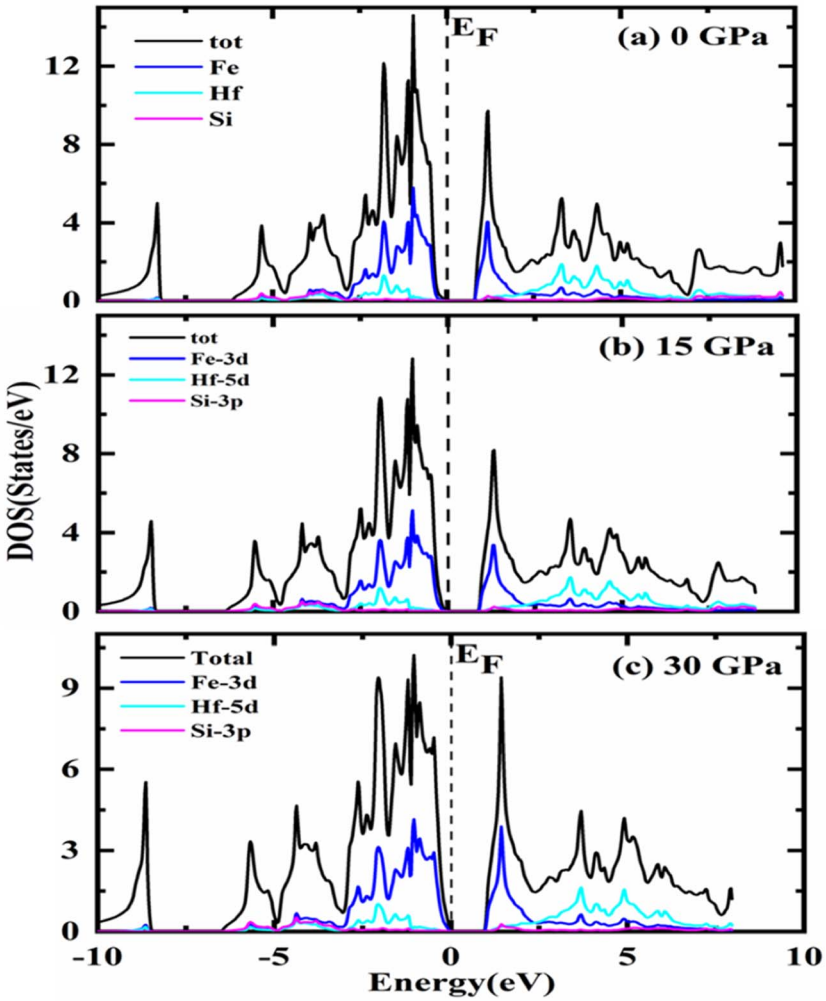

Fig. 3 DOS (total and partial density of states) of Fe_2HfSi (a) 0 GPa; (b) 15 GPa (c) 30 GPa including total DOS (in black) and the contributions of Fe-3d (in blue), Hf-5d (in cyan), Si-3p (in magenta).

index peaks shift somewhat toward higher energy values. However, various peaks may be seen in the graph centre, which disappears with higher energies. It is certain that the material transparency will be lost at a particular level of energy, and high-energy photons will be available to be absorbed at that point. Fig. 4(c) shows that the refractive index is lower than unity at specified energies. The group velocity of incoming radiation was found to be higher than the speed of light, based on lower than unity values of refractive index. It constitutes that the group velocity exposes a shift towards negative values reflecting the non-linear nature of the medium. Thus, it may be deduced that the material transforms into a superluminal medium for photons with high energies.[38,39]

Fig. 4(d) depicts a plot of extinction coefficients. It gives an idea about the light absorption and absorption characterizes the extremes of the band at the same time.[40] It is an imaginary part of the refractive index with prominent peaks probably due to the transitions among the valence and the conduction bands. At varying pressures, the reaction in Fig. 5(d) is precisely connected to the imaginary component of the dielectric function.[32] This constitutes the same trend of absorption with the same footprints of refractive index.

One of the key optical parameters used to describe how electrons are transported in the electromagnetic radiation that is being produced in the current state is called optical conductivity. This parameter obtained for a substance demonstrates its efficacy in optoelectronic devices and system applications. At various pressures, the optical conductivity of Fe_2HfSi may be shown in Fig. 5(a) as a photon energy function and we can note conductivity values are zero for energy values 0.78, 0.89, 0.90 eV at pressures of 0, 15, and 30 GPa, respectively. This is in line with the material's bandgap under varying pressures. Increasing the photon energy results in an increase in these values, which peak at 4.21, 4.42, and 4.63 eV against 0, 15, and 30 GPa pressures, respectively. It is possible to observe that the peak moves into the higher energy zone as the pressure continues to grow up to 30 GPa. After securing peak values, the graph starts showing a decreasing trend with a further increase in the energy of the photon. Practically, the optical conductivity line form is similar to that of the extinction coefficient and

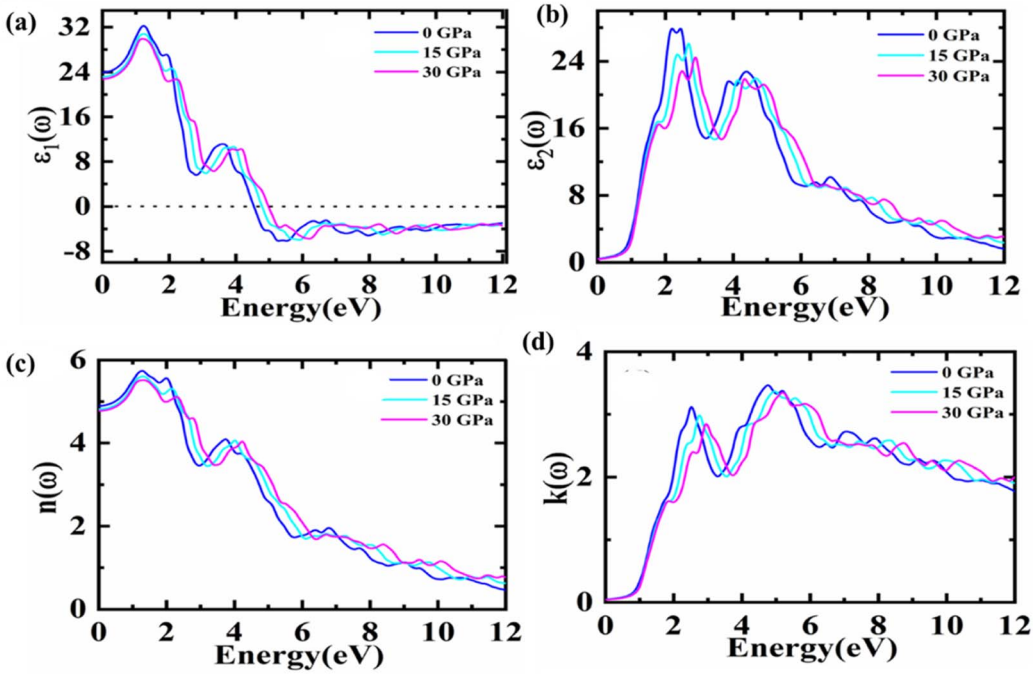

Fig. 4 Complex dielectric function (a) real, (b) imaginary part and refractive index (c) real, (d) imaginary part for Fe_2HfSi at 0, 15, 30 GPa.

dielectric imaginary part spectrums. The light intensity decreases with increasing distance as it passes through a material, and this decrease is represented by the absorption coefficient. Fig. 5(b) shows the cubic Fe_2HfSi absorption coefficient in relation to the frequency at different pressure values. The energy range from 0 to 12 eV is used to describe its fluctuation. Pressures of 0, 15, and 30 GPa produce maximum maxima of 11.3, 12.02, and 12.0, respectively. It has been seen that when the pressure goes up, the absorption peak moves up, with further increasing pressure, it may go towards higher values of energy as the trend shown in the presented data. It can also be noted that no absorption is observed for photon energy less than 1 eV for this pressure range. However, with greater energy than this value, it starts increasing, which is aided by the indirect bandgap values calculated Fe_2HfSi at different pressures respectively.

Fig. 5(c) represents the energy loss function in the 0–30 GPa pressure range. The plasma resonance/plasma frequency features are depicted in the graph by the prominent peaks. In this pressure range, no energy loss has been observed for the photons with energy less than 1 eV. For further increase in photonic energy, energy losses start increasing and come to the maximum value in the 10.3–11.12 eV energy range for 0–30 GPa, respectively. Peak shifts toward higher energies are observed by increasing pressure up to 30 GPa. An interface between the metallic and dielectric expressions may be found in the observed data.

The zero frequency limits of reflectivity shown in Fig. 5(d) also demonstrate a rise with increasing pressure and the potential to achieve an optimal value. In comparison, the energy range from 0 to 11 eV has the lowest reflectivity due to collective plasma resonance. Additionally, the imaginary part of the dielectric function can account for plasma resonance.[41] This pattern is consistent with the dielectric function imaginary portion as the reflectivity peak changes toward greater energy when the pressure is increased.[33,34] The energy loss spectrum, which is often significant at plasma energies, depicts the energy loss of a fast-moving electron through a material. It is known that the frequency associated with the peak in the loss function is the plasma frequency. These bumps correlate to the spectrum's uneven edges.

Table 3 The calculated bandgap and lattice constant at pressure 0, 15, 30 GPa for Fe_2HfSi

			Bandgap (eV)		
Compound	a (Å)	Pressure (GPa)	PBE-GGA	mBJ-GGA	Nature of bandgap
Fe_2HfSi	5.9002	0	0.317	0.828	Indirect
	5.7982	15	0.381	0.912	
	5.7032	30	0.440	0.982	
Other studies			0.590 (ref. 22)	0.40 (ref. 30)	

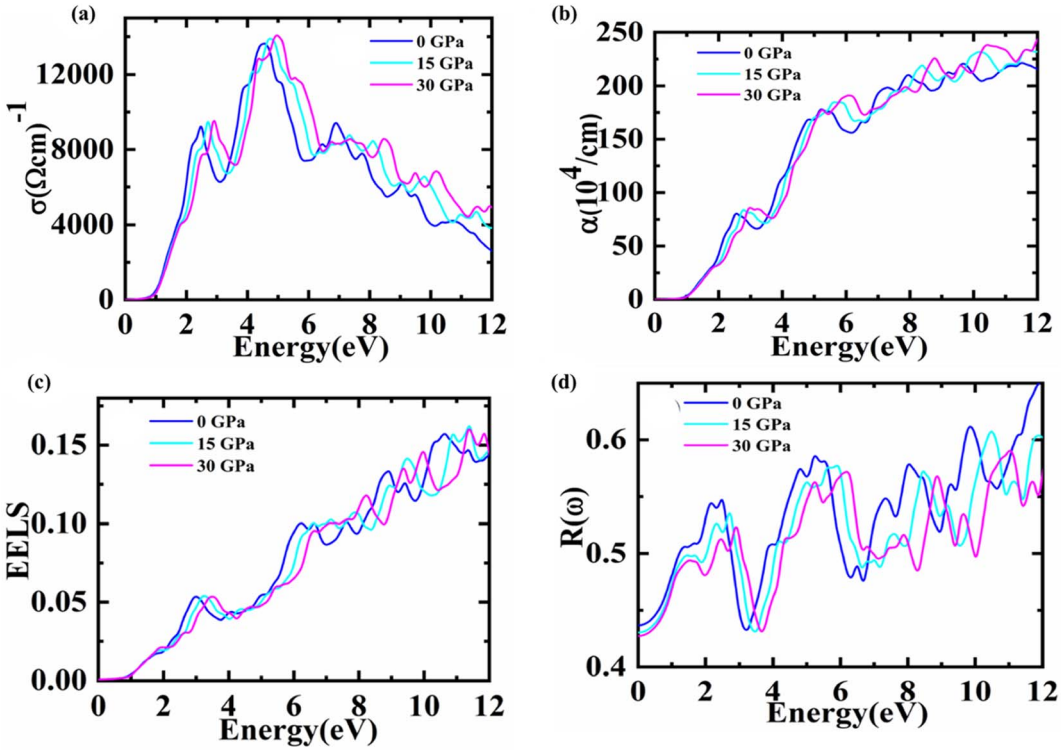

Fig. 5 For Fe_2HfSi (a) optical conductivity (b) absorption coefficient (c) EELS and (d) reflectivity data is plotted at 0, 15, 30 Gpa.

3.5. Thermoelectric properties

There is a solution to the current energy crisis in TE materials, which turns lost heat energy into functional electricity. Because of their competence and environmentally friendly energy management, such a diversity of materials is presently being investigated more quickly than other technologically notable materials. Waste heat reuse is one of TE's many innovative uses that makes them highly sought after for conserving or reducing fuel usage, notably in transportation.

Semiconductors have a substantial Seebeck coefficient (S) that is highly reliant on DOS in the vicinity of the E_F. The computed S for Fe_2HfSi as a function of temperature is shown in Fig. 6(a). The band structure study anticipated that holes (p-type) would be the dominant charge carriers for the material in the temperature range of 150–1200 K, and this is supported by the positive Seebeck coefficient. Additionally, Fe_2HfSi has a higher S than other Fe-based Heusler alloys.[42,43] Because of this, the Seebeck coefficient and indirect band gap of these alloys are rather large. Aiming for a high S value to obtain a high-efficiency TE and a close ZT is a fruitful endeavor. Utilizing the electrical conductivity and S, it gets the stuff. The charge packets must be either p/n type. We estimated the S *versus* chemical potential at various pressures, generally up to 30 GPa, to increase the performance of TE. Fig. 7(a)–(c) demonstrates that S is entirely boosted in the area where $\mu - E_F = 0$, indicating that a sufficiently large S value may be obtained with a lower p or n-type of doping. Therefore, we should emphasize whether the material's conductivity in the Fermi zone is n or p-type. This setting controls the number of transporters in the lead position. It presents n-type materials with a negative S value and p-type materials with a positive S value. Therefore, both p and n doping types are optimal for attaining a high S value. As pressure rises, the Seebeck coefficient falls, showing that Fe_2ZrSi is an excellent thermoelectric material.

The electrical conductivity parameter, which is carrier concentration-dependent, is presented in Fig. 6(b). The electrical conductivity of cubic Fe_2HfSi was measured at a spectrum of pressures and temperatures (ranging from 150 to 1200 K). It shows how many conduction-ready electrons are available. A semiconductor's band structure determines its electrical conductivity, with the most important factors being the kind and concentration of carriers, as well as the band gap.[44] Fig. 6(b) illustrates that a rise in temperature and pressure causes an increase in electrical conductivity. In the pressure range of 0–30 GPa, there is an exponential increase in conductivity as temperature rises. Despite the fact that electrical conductivity increases with pressure from 0 to 15 GPa, the maximum value of electrical conductivity is found at 30 GPa and 1200 K. Where there will concentration high results in high electrical conductivity. As per the reported data with an increase in pressure, electrical conductivity goes high for that material. Electrical conductivity is shown in Fig. 7(d)–(f) in relation to chemical potential while pressures range from 0 to 30 GPa. The graph shows that the alloy is very effective in making TE systems work well. At zero chemical potential, the electrical conductivity is at its lowest, and it goes up as the chemical potential goes up. For n-type doping, the highest level of electrical conductivity is seen.

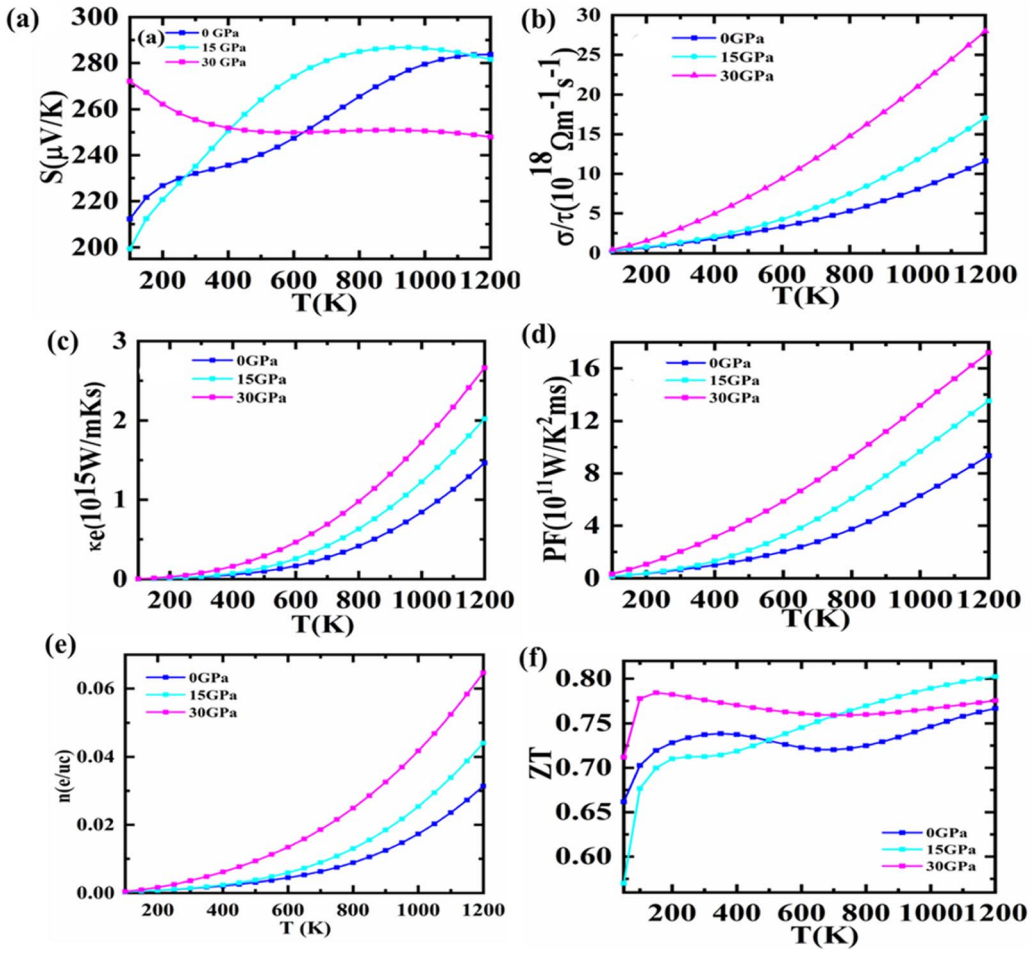

Fig. 6 Thermoelectric properties *versus* temperature in Kelvin of Fe_2HfSi are calculated (a) Seebeck coefficient, (b) electrical conductivity (c) thermal conductivity (d) power factor, and (e) total no. of charge carriers (f) figure of merit.

The phase of the material changes because the pressure goes up as the temperature goes up.

Furthermore, the electronic thermal conductivity of a material is an important thermoelectric property that fluctuates with chemical potential and affects the material's TE response. It is shown in Fig. 7(c) that how the predicted electronic thermal conductivity changes with the change in chemical potential ($\mu = \mu - E_F$) at various temperatures. It can be seen from the graph that as the temperature rises, the thermal conductivity of electrical components increases significantly. At 1200 Kelvin, κ_e/τ has attained its maximum value, whereas, at 300 Kelvin, it has dropped to its minimum. Even though there are no theoretical or experimental numbers to compare it to, the present change in the electronic thermal conductivity with chemical potential demonstrates that it is comparable to other Heusler alloys.[45,46] However, it is based on the concentration of electronic contributions. The electronic part of thermal conductivity is under consideration because of the omission of its lattice part due to high-temperature ranges.

Power factor is a dynamic tool that shows how well TE materials work. It is written as $S^2\sigma$. For a huge power factor to be reached, both σ and S must be high. At pressures from 0 to 30 GPa, the effect of chemical potential between −2 eV and 2 eV on the power factor was looked at. The results are shown in Fig. 7(j)–(l). Around −1.57 GPa, the PF goes up very quickly, and slight changes have been seen as the pressure goes from 0 to 30 GPa, but it does not go any higher than 4 GPa. Nonetheless, the best PF could be reached with p-type doping carriers. Although for the n-type doping carrier, a PF as large as p-type is unattainable, and the optimal value is challenging to achieve experimentally.[47] Fig. 7(e) shows the variation of charge carrier concentration with temperature. The increasing trend suggests charge carrier concentration increases with an increase in temperature and pressure. The figure of merit (ZT) used to determine the efficiency of TE materials is based on four variables: absolute temperature, electrical conductivity, Seebeck coefficient, and thermal conductivity. A dimensionless number that has a direct relationship with the S and an inverse relation with K. Materials that have a high S value and low K values are more efficient. The largest ZT value reported is 0.80 at 15 GPa. At 30 GPa, rather than 0 or 15 GPa, the ZT value of the proposed compound is larger at ambient temperature, as observed in

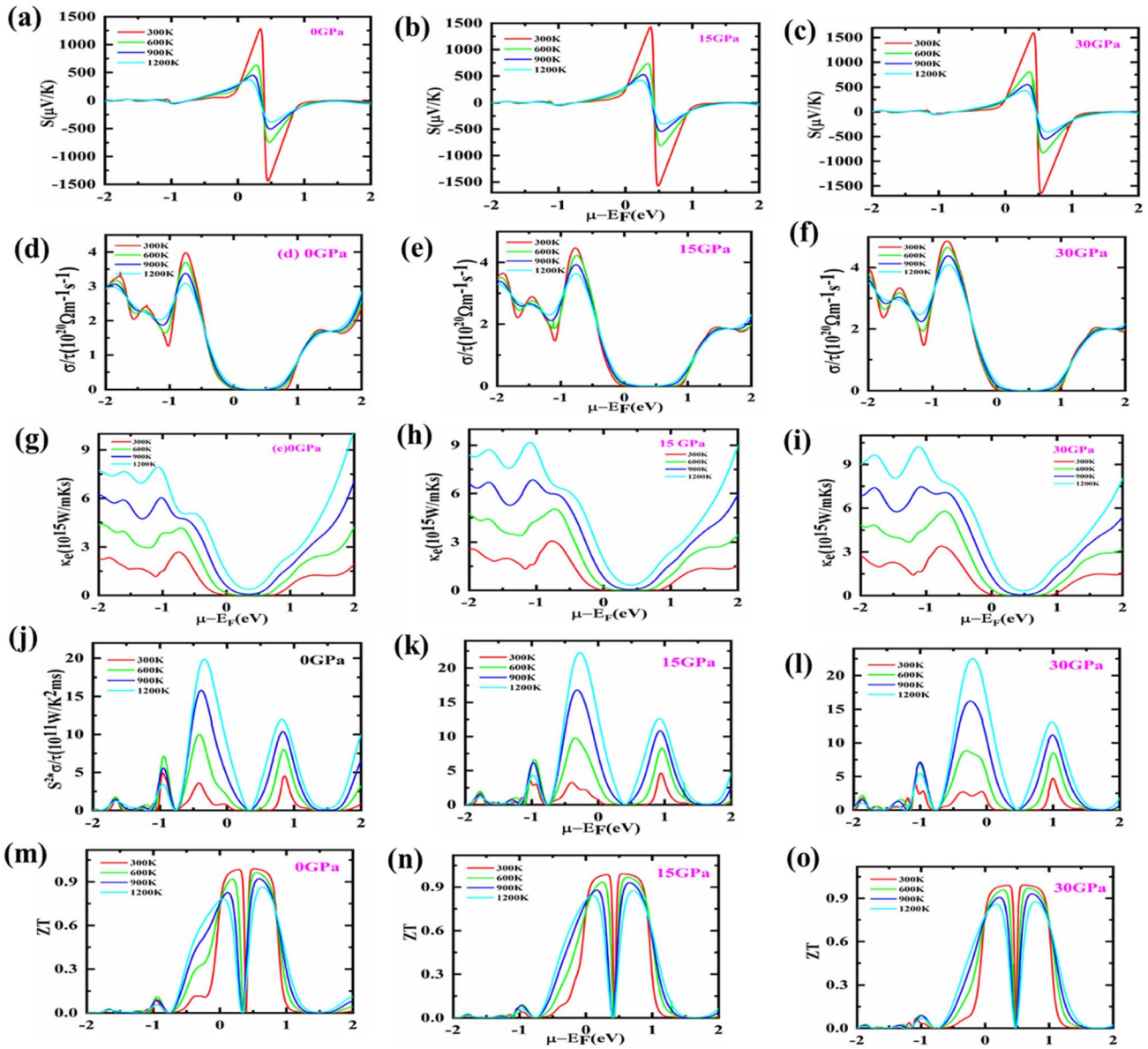

Fig. 7 The variation of (a–c) Seebeck coefficient, (d–f) electrical conductivity (g–i) thermal conductivity (j–l) power factor, and (m–o) the figure of merit with chemical potential of Fe_2HfSi alloy at different values of pressures.

Fig. 6(e). As shown in Fig. 7(m)–(o), *ZT* climbs fast as the chemical potential approaches its maximum value. At a specific chemical potential, it is stable over a broad range of chemical potentials before rapidly dissipating. *ZT* appears to be close to unity (~1) for the investigated material at all tested temperatures. In n-type regions, however, this response to a higher *ZT* is more prominent.

4. Conclusions

Fe_2HfSi pressure-induced calculations were performed using density functional theory with FP-LAPW and the modified Becke–Johnson potential (TB-mBJ). Thermal, chemical, and pressure-dependent properties of the material were taken into account in the calculation of the band structure and density of states. The stability of the cubic phase with the $Fm\bar{3}m$ space group was supported by optimization. Pressure has a tendency to widen the band-gap. At 30 GPa, band gaps can reach a maximum of 0.98 eV. A linear increase in pressure to 30 GPa results in a decrease in the static dielectric constant, plasma frequency, and static refractive index. In spite of this, pressure-induced increases in optical bandgap are consistent with Penn's model. The positive refractive index indicates that Fe_2HfSi has not become metamaterial at this pressure. Under extreme pressure, the material shows no stability in terms of plasma frequency, which has been found to rise in frequency as pressure increases. The suggested results could be extremely valuable in understanding and developing optoelectronic devices based on Fe_2HfSi under severe pressure settings. The power factor and Seebeck coefficient of Fe_2HfSi are precisely

determined by the material's unique composition. As a result, understanding how temperature and pressure affect *ZT*'s maximum value will be critical in the coming years. Understanding the doping contribution of half of Heusler alloys requires an understanding of chemical potential dependence. This type of material is in high demand for TE harvesting technologies.

Conflicts of interest

There are no conflicts to declare.

Acknowledgements

The authors express their gratitude to Princess Nourah bint Abdulrahman University Researchers Supporting Project number (PNURSP2023R61), Princess Nourah bint Abdulrahman University, Riyadh, Saudi Arabia.

References

1 T. M. Tritt and M. A. Subramanian, Thermoelectric materials, phenomena, and applications: a bird's eye view, *MRS Bull.*, 2006, **31**, 188–198.
2 C. J. Vineis, A. Shakouri, A. Majumdar and M. G. Kanatzidis, Nanostructured thermoelectrics: big efficiency gains from small features, *Adv. Mater.*, 2010, **22**, 3970–3980.
3 H. J. Goldsmid and R. W. Douglas, The use of semiconductors in thermoelectric refrigeration, *Br. J. Appl. Phys.*, 1954, **5**, 386.
4 Y. Lee, S.-H. Lo, J. Androulakis, C.-I. Wu, L.-D. Zhao, D.-Y. Chung, T. P. Hogan, V. P. Dravid and M. G. Kanatzidis, High-performance tellurium-free thermoelectrics: all-scale hierarchical structuring of p-Type PbSe–MSe Systems (M= Ca, Sr, Ba), *J. Am. Chem. Soc.*, 2013, **135**, 5152–5160.
5 Y.-L. Pei and Y. Liu, Electrical and thermal transport properties of Pb-based chalcogenides: PbTe, PbSe, and PbS, *J. Alloys Compd.*, 2012, **514**, 40–44.
6 G. Rogl, A. Grytsiv, F. Failamani, M. Hochenhofer, E. Bauer and P. Rogl, Attempts to further enhance ZT in skutterudites via nano-composites, *J. Alloys Compd.*, 2017, **695**, 682–696.
7 X. Shi, J. Yang, J. R. Salvador, M. Chi, J. Y. Cho, H. Wang, S. Bai, J. Yang, W. Zhang and L. Chen, Multiple-filled skutterudites: high thermoelectric figure of merit through separately optimizing electrical and thermal transports, *J. Am. Chem. Soc.*, 2011, **133**, 7837–7846.
8 L. Huang, Q. Zhang, B. Yuan, X. Lai, X. Yan and Z. Ren, Recent progress in half-Heusler thermoelectric materials, *Mater. Res. Bull.*, 2016, **76**, 107–112.
9 S. J. Poon, D. Wu, S. Zhu, W. Xie, T. M. Tritt, P. Thomas and R. Venkatasubramanian, Half-Heusler phases and nanocomposites as emerging high-ZT thermoelectric materials, *J. Mater. Res.*, 2011, **26**, 2795–2802.
10 J. Wei and G. Wang, Thermoelectric and optical properties of half-Heusler compound TaCoSn: a first-principle study, *J. Alloys Compd.*, 2018, **757**, 118–123.
11 W. Xie, A. Weidenkaff, X. Tang, Q. Zhang, J. Poon and T. M. Tritt, Recent advances in nanostructured thermoelectric half-Heusler compounds, *Nanomaterials*, 2012, **2**, 379–412.
12 S. Chen and Z. Ren, Recent progress of half-Heusler for moderate temperature thermoelectric applications, *Mater. Today*, 2013, **16**, 387–395.
13 J.-W. G. Bos and R. A. Downie, Half-Heusler thermoelectrics: a complex class of materials, *J. Phys.: Condens. Matter*, 2014, **26**, 433201.
14 T. Zhu, C. Fu, H. Xie, Y. Liu and X. Zhao, High efficiency half-Heusler thermoelectric materials for energy harvesting, *Adv. Energy Mater.*, 2015, **5**, 1500588.
15 I. Galanakis, P. H. Dederichs and N. Papanikolaou, Slater-Pauling behavior and origin of the half-metallicity of the full-Heusler alloys, *Phys. Rev. B: Condens. Matter Mater. Phys.*, 2002, **66**, 174429.
16 S. Yousuf and D. C. Gupta, Insight into half-metallicity, spin-polarization and mechanical properties of L21 structured MnY2Z (Z= Al, Si, Ga, Ge, Sn, Sb) Heusler alloys, *J. Alloys Compd.*, 2018, **735**, 1245–1252.
17 C. Felser, G. H. Fecher and B. Balke, Spintronics: a challenge for materials science and solid-state chemistry, *Angew. Chem., Int. Ed.*, 2007, **46**, 668–699.
18 H. Luo, Z. Zhu, L. Ma, S. Xu, H. Liu, J. Qu, Y. Li and G. Wu, Electronic structure and magnetic properties of Fe2YSi (Y= Cr, Mn, Fe, Co, Ni) Heusler alloys: a theoretical and experimental study, *J. Phys. D: Appl. Phys.*, 2007, **40**, 7121.
19 S. A. Sofi, S. Yousuf, T. M. Bhat, S. Singh, A. Q. Seh, M. Nabi, S. A. Khandy, S. A. Mir, N. A. Ganie and R. A. Mir, Investigation of pressure induced phase transition and thermoelectrics of semiconducting Fe2ZrSi, in *AIP Conference Proceedings*, AIP Publishing LLC, 2020, p. 30346.
20 S. A. Khandy, I. Islam, D. C. Gupta, R. Khenata and A. Laref, Lattice dynamics, mechanical stability and electronic structure of Fe-based Heusler semiconductors, *Sci. Rep.*, 2019, **9**, 1–8.
21 S. Masuda, K. Tsuchiya, J. Qiang, H. Miyazaki and Y. Nishino, Effect of high-pressure torsion on the microstructure and thermoelectric properties of Fe2VAl-based compounds, *J. Appl. Phys.*, 2018, **124**, 35106.
22 S. A. Sofi and D. C. Gupta, Investigation of high pressure and temperature study of thermo-physical properties in semiconducting Fe2ZrSi Heusler, *Phys. B*, 2020, **577**, 411792.
23 P. Blaha, K. Schwarz, G. K. H. Madsen, D. Kvasnicka and J. Luitz, *wien2k, An Augmented Plane Wave+ Local Orbitals Program for Calculating Crystal Properties*, 2001, vol. 60.
24 J. P. Perdew, K. Burke and M. Ernzerhof, Generalized gradient approximation made simple, *Phys. Rev. Lett.*, 1996, **77**, 3865.
25 F. Tran and P. Blaha, Accurate band gaps of semiconductors and insulators with a semilocal exchange-correlation potential, *Phys. Rev. Lett.*, 2009, **102**, 226401.

26 G. K. H. Madsen and D. J. Singh, BoltzTraP. A code for calculating band-structure dependent quantities, *Comput. Phys. Commun.*, 2006, **175**, 67–71.
27 F. D. Murnaghan, *Proc. Natl. Acad. Sci. U. S. A.*, 1994, 244–247.
28 T. Gasi, V. Ksenofontov, J. Kiss, S. Chadov, A. K. Nayak, M. Nicklas, J. Winterlik, M. Schwall, P. Klaer and P. Adler, Iron-based Heusler compounds Fe 2 Y Z: Comparison with theoretical predictions of the crystal structure and magnetic properties, *Phys. Rev. B: Condens. Matter Mater. Phys.*, 2013, **87**, 64411.
29 J. Winterlik, G. H. Fecher, B. Balke, T. Graf, V. Alijani, V. Ksenofontov, C. A. Jenkins, O. Meshcheriakova, C. Felser and G. Liu, Electronic, magnetic, and structural properties of the ferrimagnet Mn 2 CoSn, *Phys. Rev. B: Condens. Matter Mater. Phys.*, 2011, **83**, 174448.
30 L. Wang, Y. Cao, C. Zhang, Y. Xu and S. Zhou, Theoretical study of structural, mechanical, electronic, magnetic and thermodynamic properties of Cu2MnAl-type Fe2YAl (Y= Cr, Mo and W) full-Heusler alloys, *Mater. Sci. Eng., B*, 2022, **278**, 115639.
31 M. Jamal, M. Bilal, I. Ahmad and S. Jalali-Asadabadi, IRelast package, *J. Alloys Compd.*, 2018, **735**, 569–579.
32 O. Anderson, E. Schreiber and N. Soga, *Elastic Constants and Their Measurements*, 1973.
33 M. Meinert, M. P. Geisler, J. Schmalhorst, U. Heinzmann, E. Arenholz, W. Hetaba, M. Stöger-Pollach, A. Hütten and G. Reiss, Experimental realization of a semiconducting full-Heusler compound: Fe 2 TiSi, *Phys. Rev. B: Condens. Matter Mater. Phys.*, 2014, **90**, 85127.
34 J. Shiomi, K. Esfarjani and G. Chen, Thermal conductivity of half-Heusler compounds from first-principles calculations, *Phys. Rev. B: Condens. Matter Mater. Phys.*, 2011, **84**, 104302.
35 D. Behera, R. Sharma, H. Ullah, H. S. Waheed and S. K. Mukherjee, Electronic, optical, and thermoelectric investigations of Zintl phase AAg2Se2 (A= Sr, Ba) compounds: A first first-principles approach, *J. Solid State Chem.*, 2022, 123259.
36 D. Behera and S. K. Mukherjee, Theoretical Investigation of the Lead-free K2InBiX6 (X= Cl, Br) Double Perovskite Compounds Using First Principle Calculation, *JETP Lett.*, 2022, 1–10.
37 V. Sharma and G. Pilania, Electronic, magnetic, optical and elastic properties of Fe2YAl (Y= Ti, V and Cr) using first principles methods, *J. Magn. Magn. Mater.*, 2013, **339**, 142–150.
38 M. Ahmad, G. Murtaza, R. Khenata, S. Bin Omran and A. Bouhemadou, Structural, elastic, electronic, magnetic and optical properties of RbSrX (C, SI, Ge) half-Heusler compounds, *J. Magn. Magn. Mater.*, 2015, **377**, 204–210.
39 G. Surucu, Investigation of structural, electronic, anisotropic elastic, and lattice dynamical properties of MAX phases borides: An Ab-initio study on hypothetical M2AB (M= Ti, Zr, Hf; A= Al, Ga, In) compounds, *Mater. Chem. Phys.*, 2018, **203**, 106–117.
40 D. Behera, M. Manzoor, M. W. Iqbal, S. Lakra and S. K. Mukherjee, Revealing Excellent Electronic, Optical, and Thermoelectric Behavior of EU Based $Euag_2y_2$ (Y= S/Se): For Solar Cell Applications, *Comput. Condens. Matter*, 2022, **32**, e00723.
41 Y. O. Ciftci and M. Evecen, First principle study of structural, electronic, mechanical, dynamic and optical properties of half-Heusler compound LiScSi under pressure, *Phase Transitions*, 2018, **91**, 1206–1222.
42 T. M. Bhat and D. C. Gupta, Robust thermoelectric performance and high spin polarisation in CoMnTiAl and FeMnTiAl compounds, *RSC Adv.*, 2016, **6**, 80302–80309.
43 S. Sharma and S. K. Pandey, Applicability of two-current model in understanding the electronic transport behavior of inverse Heusler alloy: Fe2CoSi, *Phys. Lett. A*, 2015, **379**, 2357–2361.
44 A. Jayaraman, Diamond anvil cell and high-pressure physical investigations, *Rev. Mod. Phys.*, 1983, **55**, 65.
45 K. Kaur, TiPdSn: A half Heusler compound with high thermoelectric performance, *Europhys. Lett.*, 2017, **117**, 47002.
46 T. Wu, W. Jiang, X. Li, Y. Zhou and L. Chen, Thermoelectric properties of p-type Fe-doped TiCoSb half-Heusler compounds, *J. Appl. Phys.*, 2007, **102**, 103705.
47 J. L. Baker, R. S. Kumar, C. Park, N. Velisavljevic and A. Cornelius, Compressibility and thermoelectric behavior of TiCoSb half-Heusler compound at high pressures, *Intermetallics*, 2018, **95**, 137–143.